PCCP

Femtosecond electronic relaxation and real-time vibrational dynamics in 2'-hydroxychalcone

Journal:	*Physical Chemistry Chemical Physics*
Manuscript ID	CP-ART-10-2018-006405.R1
Article Type:	Paper
Date Submitted by the Author:	05-Nov-2018

Complete List of Authors:	Yamakita, Yoshihiro; Denki Tsushin Daigaku, Department of Engineering Science, Graduate School of Informatics and Engineering Yokoyama, Nanae; Denki Tsushin Daigaku, Department of Engineering Science, Graduate School of Informatics and Engineering Bing, Xue; Denki Tsushin Daigaku, Department of Engineering Science, Graduate School of Informatics and Engineering Shiokawa, Naoyuki; Denki Tsushin Daigaku, Department of Engineering Science, Graduate School of Informatics and Engineering Harabuchi, Yu; Hokkaido University, Department of Chemistry, Faculty of Science; JST, PRESTO, Maeda, Satoshi; Faculty of Science, Hokkaido University, Department of Chemistry Kobayashi, Takayoshi; Denki Tsushin Daigaku, Brain Science Inspired Life Support Research Center; National Chiao-Tung University, Department of Electrophysics; Osaka University, Institute of Laser Engineering

Femtosecond electronic relaxation and real-time vibrational dynamics in 2'-hydroxychalcone†

Yoshihiro Yamakita,*[a] Nanae Yokoyama,[a] Bing Xue,[a] Naoyuki Shiokawa,[a] Yu Harabuchi,[bc] Satoshi Maeda,[b] and Takayoshi Kobayashi*[def]

Abstract: Femtosecond ultrafast electronic relaxation and vibrational dynamics in 2'-hydroxychalcone after deep ultraviolet (DUV) excitation were observed by two types of pump-probe spectroscopy experiments, i.e., DUV-pump pulse and visible-broadband-probe pulse (DUV/Vis) experiments and DUV-pump and DUV-probe (DUV/DUV) pulses experiments. Time-dependent density functional theory (TDDFT) calculations were performed to elucidate relaxation dynamics from the third singlet electronic excited state S_3. The DUV/Vis experiments and TDDFT calculations have disclosed the ultrafast dynamics of internal conversion from the initial S_3 state ($\tau_1 \approx 35$ fs) towards the S_1 state via a rapid process through the S_3/S_2 conical intersection and proton transfer [OH: $\tau_2(\mathrm{H}) \approx 93$ and OD: $\tau_2(\mathrm{D}) \approx 164$ fs] before deactivation through the S_1/S_0 conical intersection ($\tau_3 \approx 690$ fs). Thanks to the ultrashort pump and probe pulses, real-time observation of vibrational modes coupled to the electronic excitation was realized providing both amplitudes and phases. Spectrogram analyses were performed based on the real-time spectra obtained by the DUV/Vis experiments, in which instantaneous vibrational frequencies reflecting molecular structural change after the impulsive excitation were visualized. The vibrational frequency of central C=C bond stretch decreases from ~1600 cm^{-1} to ~1560 cm^{-1} in about 200–500 fs and recovers by ~550 fs. Normal mode analyses along the decay path support the observed variation of the C=C stretching frequency. The temporal weakening of the central C=C bond is connected with the angle of the two aromatic rings which flip back to the initial conformation.

[a] *Department of Engineering Science, Graduate School of Informatics and Engineering, The University of Electro-Communications, 1-5-1 Chofugaoka, Chofu, Tokyo 182-8585, Japan. E-mail: yamakita@uec.ac.jp*
[b] *Department of Chemistry, Faculty of Science, Hokkaido University, Sapporo 060-0810, Japan.*
[c] *JST, PRESTO, 4-1-8 Honcho, Kawaguchi, Saitama, 332-0012, Japan.*
[d] *Brain Science Inspired Life Support Research Center, The University of Electro-Communications, 1-5-1 Chofugaoka, Chofu, Tokyo 182-8585, Japan. E-mail: tkobayashi@uec.ac.jp*
[e] *Department of Electrophysics, National Chiao-Tung University, 1001 Ta Hsinchu Rd., Hsinchu 30010, Taiwan.*
[f] *Institute of Laser Engineering, Osaka University, 2-6 Yamada-oka, Suita, Osaka 565-0971, Japan.*
† Electronic supplementary information (ESI) available: Calculated geometries, energies and normal modes at crucial points, recorded Raman spectra of 2'HC and formalisms for obtaining two-photon absorption cross-sections and molar absorption coefficients of transient species are supplied. See DOI: xxx.

Keyword:
2'-hydroxychalcone, femtosecond time-resolved pump-probe spectroscopy, TDDFT, conical intersection

1. Introduction

Ultrafast time-resolved (TR) spectroscopy is a powerful tool to investigate photochemical/physical dynamics of molecular systems. This paper reports on ultrafast dynamics of deep-ultraviolet (DUV) excited 2'-hydroxychalcone (2'HC), which undergoes internal conversion involving proton transfer in the excited states. Photo-induced spectral changes are monitored based on the pump-probe scheme at different probe wavelengths. The real-time vibrational dynamics is studied by the femtosecond time-resolved spectroscopy (TRS).

Chalcone compounds, most notably hydroxychalcone derivatives, are abundant in nature and reported to show rich pharmacological activity such as antibacterial and antioxidant activities.[1-3] In particular, 2'HC undergoes *cis-trans* photoisomerization and subsequent dehydration reaction to give flavanone, as shown in Fig. 1(a), where the OH group plays an important role. The photochemistry of 2'HC analogues has been studied extensively in the last three decades.[4-6] Favanone is an oxidized form of flavan, which is the basic skeleton of the vast family of flavonoid. The flavonoid family[7] includes many kinds of metabolites of plants, such as flavanone, flavone, catechin, and anthocyanidin. Glycosides of anthocyanidin, anthocyanin, are origins of various colours of flowers and fruits under specific pH conditions.[8] Therefore, a TR study on chalcone compounds would provide a basic demonstration on the photodynamics in natural organic chemistry.

The photodynamics of the 2'HC compounds has been studied previously by several research groups using time-dependent or transient absorption experiments. Matsushima *et al*. have systematically studied the photocyclization processes of substituted 2'HC in various solvents using excitation by a high-pressure Hg lamp, and determined the quantum yields of photoproducts.[4] Chou *et al*. have also studied transient species using UV-laser excitation,[5] and Norikane *et al*. have reported nanosecond flash photolysis experiments in various solvents together with semi-empirical calculations.[6] These studies have clarified that the photochemical reactions in Fig. 1(a) are initiated by the excited-state intramolecular-proton transfer (ESIPT) followed by the S_1-T_1 intersystem crossing.[5,6] However, the TR absorption spectra recorded in these experimental studies[5,6] are limited in the delay time range longer than ~60 ns. Any ultrafast dynamics of 2'HC has not been elucidated in picosecond or femtosecond time regimes. The available semi-empirical calculations[6] are only for the S_1 and T_1 states, and *ab initio* quantum chemical calculations are desired at sophisticated levels.

With femtosecond time resolution, the ultrafast electronic relaxation processes and vibrational wavepacket dynamics can be observed simultaneously. Especially, the latter allows direct observation of the amplitudes of vibrational modes which are coupled to the impulsively-triggered electronic transition by a femtosecond pulse. This methodology is the real-time vibrational spectroscopy (RTVS) and advantageous over conventional TR vibrational spectroscopies including TR infrared (IR)-absorption and TR Raman spectroscopies. These cannot provide vibrational phase information. Furthermore, RTVS can provide the information of 'instantaneous' vibrational frequencies via

spectrogram analysis (SA) using gated Fourier transform (FT) of the real-time traces. These methods, RTVS and SA, clarify various ultrafast phenomena in photochemical processes including *cis-trans* isomerization,[9] Claisen rearrangement.[10] Varieties of photophysical processes have also been observed such as dynamic vibrational mode coupling,[11] chirping of molecular vibrational frequency,[12] dynamic Duschinsky rotation[13] and time-dependent Herzberg-Teller coupling.[14,15]

In contrast to 2'HC, 2-hydroxychalcone (2HC) analogues which possess the OH group at the other ring [see Fig. 1(a) for atom numbering] undergo cyclization to give strongly-coloured flavylium (anthocyanidin) compounds.[16,17] In general, the chalcone analogues exhibit UV absorption at about 390 nm whereas the flavylium analogues show absorption in a visible (Vis) region around 540 nm. Related to the cyclization reaction which gives the basic unit of anthocyanidin, Pina and co-workers have studied the photodynamics of a 2HC analogue, 4-(dimethylamino)chalcone, using picosecond TR absorption spectroscopy,[17] and proposed a solvent-dependent photoisomerization process involving proton-transferred intermediate species that are produced after *trans-cis* isomerization. The proton transfer is mediated by solvent water.

The distinct absorption change upon cyclization from chalcone to flavylium analogues can be used as a molecular switching system.[18] Namely, *trans*-2-hydroxy-4'-methoxy-chalcone photoisomerizes to the *cis* form ('write' by photons), and preferentially interconvert towards 4'-methoxy-flavylium cation at low pH < 1 ('lock'). The different UV (~390 nm) and Vis (~540 nm) absorption bands of the chalcone and flavylium compounds prevent a reverse photoreaction. The written state is stable unless pH is increased. The hydration reaction by increasing pH > 1 will 'unlock' the cationic state, and the *cis-trans* backward reaction will 'erase' the switched state.

The radiative and non-radiative decay mechanisms of other chalcone derivatives have also been studied extensively,[19-21] in which locally excited (LE) and twisted intramolecular charge-transfer (TICT) states are involved. The fluorescence quantum yields and energy levels of all-planar emissive LE state (E*), C-C bond-twisted more-emissive TICT polar state (A*) and C=C bond-twisted less-emissive biradical state (P*) have been discussed in relation with conical intersections between them.[20] Mechanistic and solvatokinetic effects which stem from the C=C bond twist have also been discussed.[19,20] The internal rotation in the ground and excited states of substituted stilbene[22] and ketone[23] as well as chalcone and C=C/C-C bridged analogues[24,25] have been basic model systems in the photochemistry of π-conjugated systems.

In this paper, we present multichannel TR absorption spectroscopy experiments in the femtosecond time regime for *trans*-2'HC. After 2'HC absorbs a 9-fs DUV pump pulse, it undergoes photochemical/photophysical processes until it returns to the electronic ground state or reaches flavanone through the multiple processes.[4] The DUV pulse duration of 9 fs is the world shortest ever used for TR spectroscopy except in our previous two papers.[26,27] Based on experimental and theoretical results, we discuss the ultrafast relaxation and vibronic processes on the electronic excited state surfaces. We demonstrate experimental determination of wavelength-dependent lifetimes and absolute molar

absorption coefficients of transient species. The two types of experiment are performed; the DUV pump/Vis probe (experiment A) and DUV pump/DUV probe experiments (experiment B).

2. Experimental

Our experimental setup has been reported previously.[26,28,29] Briefly, the ultrafast TR difference absorption/emission spectra [$\Delta A(\lambda, t_d)$] are recorded using a polychromator coupled to a 128-channel lock-in amplifier (MCLIA) and a piezo-controlled optical delay stage. The multi-channel detection at 128 different probe wavelengths λ at delay time t_d accumulates the difference absorbance signal as ΔA with pump on and off. Thus, two-dimensional (2D) spectra $\Delta A(\lambda, t_d)$ of RTVS are obtained as contours on the 2D map. The ΔA spectra in the Vis or DUV regions monitor ultrafast electronic relaxations and real-time amplitudes of vibrations coupled to the corresponding electronic states at relevant t_d.

The multiplex capability for different wavelength has experimental advantages over single-wavelength detection by several factors, since it can trace electronic and vibrational dynamics at the same time. The advantages are listed in detail as follows.

(1) Experimental errors due to inevitable laser intensity fluctuations and spectral change due to various non-linear optical processes in the DUV pulse generation stage can be significantly reduced.

(2) Data taking time for the multichannel experiments is reduced by more than 100 times from single channel experiments.

(3) Mechanical and temperature instability that a large number of optical components in the system could suffer from can be minimized.

The intensity fluctuation and spectral change of the ultrashort DUV pulse system in (1) arises from the multiple nonlinear optical (NLO) pulse generation mechanisms including the self-phase modulation, self-focusing, stimulated Raman gain and loss, the parametric four-wave mixing and supercontinuum generation.[30]

Further advantage is that the 2D map of $\Delta A(\lambda, t_d)$ can elucidate both behaviors of intensity dynamics and spectral change. That is, quantitative analyses of the ΔA contour map allow reliable determinations of the ultrafast dynamics in case of 'cross-talk' between the intensity change at some specific spectral components (we call this vertical change) and spectral shift (horizontal change). Single-channel analyses cannot discriminate such a spectral change from a temporal change.

A 798 nm fundamental-frequency output from a Ti: sapphire regenerative amplifier (35 fs, 798 nm, 3 mJ, 1 kHz) is separated into two beams for the purpose of generating the DUV pump pulse (260–280nm) and the Vis broadband probe pulse (500–650 nm) in experiment A. The DUV pulse is used also as the probe pulse in experiment B as mentioned above.

One of the two split fundamental-frequency pulses is used to generate the DUV pump pulse as follows. It is separated into two beams again. One beam is frequency doubled in a BBO (beta barium borate, β–BaB_2O_3) crystal to produce 399 nm pulse and then negatively chirped by diffraction with a

grating pair two times. The other beam is focused into a Kr-filled hollow-core fiber and converted to positively-chirped near-infrared (NIR) supercontinuum by the self-phase modulation. The amount of positive chirp is adjusted with chirped mirrors. Both of the beams are finally overlapped spatially and temporally in an Ar-filled hollow core fiber, and converted to a chirped DUV pump pulse based on the parametric four-wave mixing scheme. The maximal spatial overlap of the beams in the Ar-filled hollow core fibers is attained with piezo-controlled feedback mirrors by utilizing the intensity of reduced DUV pulse as an error signal. The negative group-velocity dispersion of the DUV pump pulse is compensated by travelling through air, resulting in nearly FT-limited FWHM (full width at half maximum) duration of 9 fs. The time resolution of the TR measurements is estimated to be ~12 fs from time convolution of the pump and probe pulses.

The other separated fundamental-frequency pulse is spectrally broadened by focusing into a 2-mm thick sapphire plate and converted to a Vis-to-NIR broad-band probe pulse by supercontinuum generation including self-phase modulation and other NLO processes The intensity and spectrum are optimized to obtain a stable clean ultrashort pulse by adjusting a variable neutral density filter placed in front of the sapphire plate.

The multichannel detected probe signal is recorded at each delay time t_d. The optical delay is controlled stepwise by a translation stage that holds a pair of mirrors perpendicularly. The probe pulse after a sample cell is guided through a bundle fiber towards a polychromator, in which the probe pulse is dispersed by a grating [Vis: 300 grooves/mm and 500-nm bandwidth (BW); DUV: 1800 grooves/mm and 300-nm BW]. The multi-colour signals are detected by 128 avalanche photodiodes that are aligned parallel to the spectral dispersion. The output signal is coupled to the 128-channel multi-channel lock-in-amplifier (MCLIA) through a multi-mode fiber bundle. The MCLIA is operated with the time constant of 3 s. The signals are accumulated as a 2D map of difference absorbance[31] $\Delta A(\lambda, t_d)$ using a mechanical chopper operated at 1 kHz. The lock-in detection is performed in synchronous with the chopper through a low-pass filter.

A methanol solution sample of *trans*-2'HC is spewed into a 0.5-mm thick cell which is connected to a circulating pump through a tube. This setup makes it possible to avoid optical or thermal damages. The circulation speed is adjusted for a sample solution in a focused volume not to experience double excitations. The concentration of the sample is 0.1 and 0.01 mol/L for the Vis and DUV probes, respectively. The latter concentration is optimized for the transmitted probe DUV light to be intense enough for detection with a high signal to noise ratio. Typical pulse energies of the pump and probe are 90 and 10 nJ, respectively. The static electronic absorption spectra of 2'HC are recorded using a UV/Vis spectrometer (Shimadzu UV-3101). The H/D substitution of deuterated 2'HC is confirmed by NMR experiments in CCl_4 solutions.

The group velocity dispersion (GVD) in any media broadens the pulse duration. However, as long as the penetration depth of the *pump* pulse into the media (solution in this case) is sufficiently small, the time resolution of ΔA is effectively unchanged since the induced ultrafast phenomena that contribute

to Δ*A* take place within the depth. The thickness of the cell can thus be arbitrarily selected if the probe pulse is intense enough to be detected after passing through the cell. In the present experiments the DUV pump or DUV probe pulse is strongly absorbed by 2'HC,[6] whereas the Vis probe pulse is transparent to the solvent and 2'HC and can be absorbed only by transient species.

The intensity I of light in the linear absorption regime is attenuated exponentially as a function of the path length l, and the penetration depth δ_p is defined to be the inverse of the absorption coefficient α:

$$I(l) = I_0 e^{-\alpha l}, \quad (1)$$

$$\delta_p = \frac{1}{\alpha}. \quad (2)$$

Comparison with the Lambert-Beer law gives a relation of δ_p with the molar absorption coefficient ε and concentration c:

$$A = -\log_{10}\left(\frac{I}{I_0}\right) = \varepsilon c l, \quad (3)$$

$$\delta_p = \frac{1}{\varepsilon c \ln 10}. \quad (4)$$

Using the expression of δ_p in Eq. (4), the GVD broadening of the DUV pump pulse can be estimated. The GVD of methanol is 229.76 fs^2/mm and ε of 2'HC is 0.50×10^4 mol^{-1}L cm^{-1} at 270 nm.[6] The shorter- and longer-wavelength edges of the pump pulse are located around 260 and 280 nm, respectively, as in Fig. 1(b). Using the concentration 0.1 mol/L of 2'HC for the Vis probe experiments, the penetration depth of the DUV pump pulse is estimated to be δ_p = 8.7 and 5.8 μm at 260 and 280 nm, respectively. Corresponding GVD broadening is only 0.20 and 0.13 fs, being almost negligible. In the case of the DUV probe experiments, these values are one order magnitude larger due to the low concentration of 0.01 mol/L. Nonetheless, the broadening of the 260 and 280 nm components of the pump pulse is only 2.0 and 1.3 fs, respectively.

The total attenuation factors of the DUV probe pulse after transmitted through the 0.5 mm thickness are calculated to be 3.2×10^{-3}, 1.8×10^{-3} and 0.2×10^{-3} at the wavelengths 260 nm, 270 nm and 280 nm, respectively, from the molar absorption coefficients 0.50×10^4, 0.55×10^4 and 0.75×10^4 mol^{-1}L cm^{-1}.[6] These values correspond to the absorbance of ~3, and the attenuated probe pulse can still provide a sufficient intensity to be detected. The attenuation of the Vis probe pulse is almost negligible as noted above.

3. Computational details

Calculations of the usual linear-response time-dependent density functional theory (TDDFT)[32,33] are performed to elucidate the molecular deformations and decay dynamics of 2'HC in the electronic

excited states after photoexcitation to the S_3 state. Critical points are optimized along the decay path departing from the initial structure (denoted by S_{3FC}) under the Franck-Condon approximation towards the conical intersection between the first excited and the ground electronic states (denoted by S_1/S_0). The connectivity of the critical points is confirmed by following intrinsic reaction coordinates (IRC) and meta-IRCs (the steepest descent path in the mass-weighted coordinate).[34] In the TDDFT calculations, the ωB97XD functional[35] is employed along with the 6-31G(d) basis set, because the ωB97XD functional is known to be one of the best choices to describe excited states by the TDDFT calculations.[36] As a result, the present calculations are in good agreement with the experimental observation. It is recalled that the TDDFT calculation in general provides only a qualitative description of the excited states.

Normal mode analyses are applied to several potential minima in methanol and utilized to investigate the decay dynamics and deformation components along the decay path. The S_0/S_1 geometry is optimized by using spin-flip TDDFT (SF-TDDFT) calculations.[37-39] Also, the most energetically preferred decay channels are systematically searched by using the seam model function (SMF) / single component artificial force induced reaction (SC-AFIR) method[40,41] with the SF-TDDFT method in the vacuum. In the SMF/SC-AFIR search, eleven atoms around C1', i.e. C1', C2', C3', C6', O11, H14, O10, C9, H13, C8 and C7 are accounted as the target atoms for the SC-AFIR scheme.[42] In the SF-TDDFT calculations, the BHHLYP functional[43,44] with the 6-31G(d) basis set is used.

The solvent effect on the decay path is examined for 2'HC in methanol compared to that in the vacuum. All of the optimized structures in methanol and in the vacuum are shown in Table S1 and S2. The solvent effect is taken into account using the CPCM (conductor-like polarizable continuum model)[45-48] TDDFT energies and gradients are computed using the Gaussian 09 program package,[49] and SF-TDDFT energies and gradients are obtained using the GAMESS program package.[50,51] All of geometry optimizations, meta-IRC calculations and the SMF/SC-AFIR search are performed by using a developmental version of the GRRM (Global Reaction Route Mapping) program.[52]

4. Results and Discussion

4.1 DUV pump – Vis-NIR probe experiments

Fig. 1(b) shows the electronic absorption spectrum of *trans*-2'HC in methanol. The observed peak at ~3.9 eV and shoulder at ~3.5 eV are assigned, respectively, to the transitions from S_0 to $S_3(\pi_2\pi^*)$ and from S_0 to $S_1(\pi_1\pi^*)$ based on the calculated oscillator strengths, 0.99 for S_1 ($\pi_1\pi^*$), less than 0.001 for S_2 ($n\pi^*$) and 0.24 for S_3 ($\pi_2\pi^*$) in methanol. These transitions are approximately described as one-electron promotion among molecular orbitals π_1, π_2, n and π^*. The transition energies are calculated to be 3.81 eV (S_1), 3.96 eV (S_2) and 4.21 eV (S_3) in methanol. Thus, the present pump energy centered at ~4.7 eV (260–280 nm) is located in post resonant with the $S_3 \leftarrow S_0$ absorption, as shown in Fig. 1(b). The present assignments are in line with the previous papers that have reported absorption and emission

spectra in various solvents for *trans*-2'HC, *cis*-2'HC and flavanone along with semi-quantitative calculations.[4-6,53]

The Vis probe pulse in the energy range 1.9–2.6 eV (480–640 nm) is not resonant with the absorption from the ground state of *trans*-2'HC in Fig. 1(b). Therefore, negative ΔA due to bleaching of the $S_3 \leftarrow S_0$ absorption will not appear in the Vis probe experiments. If *trans*-2'HC is converted to the triplet state, negative ΔA due to the Vis emission could in principle contribute in this visible range (Fig. 3 in Ref. 6). However, the time scale of the intersystem crossing is ~1 μs, which is far beyond the femtosecond time scale. Multiphoton ionization is unlikely under the present condition, since the ionization energy of aromatic molecules[54] normally larger than 8 eV and the two-photon absorption crossections of typical organic conjugated molecules are of the order of σ_{TPA} = 6000 GM (Göppert-Mayer unit, 10^{-50} cm^4 s photon^{-1}).

In the present study, the concentrations of the sample are $C_{Vis} = 6.02\times10^{19}$ molecule cm^{-3} (0.1 mol/L) for the Vis probe experiments and $C_{DUV} = 6.02\times10^{18}$ molecule cm^{-3} (0.01 mol/L) for the DUV probe experiments. Using σ_{TPA} and δ_p, the attenuation by two-photon absorbance ΔI_{Vis} of the pump pulse in the Vis probe experiments is estimated to be $\Delta I_{Vis} = 4.99\times10^{23}$ photon cm^{-2} s^{-1}. This attenuated photon flux is negligible compared to the incident photon flux, $I_0 = 4.88\times10^{27}$ photon cm^{-2} s^{-1}. Details are given in the Electronic Supplementary Information (ESI).

Fig. 2(a) presents a 2D difference absorption spectrum $\Delta A(\lambda, t_d)$ [or equivalent $\Delta A(\omega, t_d)$] between S_3-photoexcited and unexcited methanol solution of 2'HC in the delay time range from −440 fs to 1700 fs. The horizontal stripes on the central part of the contour map are not due to mechanical noise induced by the non-smooth stage motion which is carefully ruled out by blank-test experiment without a sample. It is attributed to temporal modulation of electronic spectra by coupled molecular vibrations that are induced impulsively by the pump pulse with duration shorter than the vibrational period. The temporal modulation of electronic transition probability between the ground and excited states is induced by the vibrational modes via vibronic coupling. From the FT of $\Delta A(\lambda, t_d)$ over a delay time range, we can obtain the vibrational frequencies of the coupled modes. The impulsively excited vibrational motion also induces the modulation of refractive index of transparent solvent by the non-resonant impulsive Raman effect. In fact, the FT of the time-dependent $\Delta A(\lambda, t_d)$ traces gives the vibrational frequencies of decaying 2'HC and the Raman-active vibration of methanol at 1035 cm^{-1}. Details are discussed in Section 4.8.

Fig. 2(b) shows TR difference transient absorption spectra $\Delta A(\lambda, t_d)$ at nine delay times in the probe range 1.95–2.60 eV (633–475 nm), whereas Fig. 2(c) are time dependences of difference absorbance at four wavelengths. The most prominent change in Fig. 2(b) is the abrupt decrease observed from 0 to 100 fs over almost entire frequency region. The following phenomena can be understood in terms of energy regions above and below ~2.25 eV. The intensity of the higher energy band above 2.25 eV

decreases gradually, whereas the lower energy band below 2.25 eV gains the intensity again from delay time $t_d \approx 100$ fs (red) and levels off towards ~500 fs (green). It decreases again after ~500 fs. These TRS suggest the existence of (a) a slow decreasing spectral component towards ~1000 fs in the region above 2.25 V and (b) fast decreasing components in a short delay time up to ~100 fs and following slower increasing components over 500~1000 fs below 2.25 eV.

To investigate the complicated behaviour more clearly, the time dependences of ΔA are shown in Fig. 2(c) at probe photon energies 2.42 eV (512 nm), 2.33 eV (532 nm), 2.25 eV (551 nm) and 2.09 eV (594nm). The traces show remarkable differences among them. Namely, ΔA at 2.42 eV seems to decrease with two decay constants before and after ~200 fs. On the other hand, ΔA at 2.25 and 2.09 eV display a sharp rise and fall around t_d = 0–100 fs, and a gradual increase towards ~500 fs. These behaviours above and below 2.25 eV correspond to the slow process (a) and fast processes (b) mentioned above, respectively.

In principle, difference absorbance ΔA can become positive or negative depending upon competitive contributions from absorption or stimulated emission. It can be reduced by population depletion of the initial state as well. Since ΔA in the probe energy range of 1.95–2.60 eV does not overlap with the S_0 absorption shown in Fig. 1(b), the observed ΔA is predominantly attributed to absorption or stimulated emission from transient excited states. The observed positive ΔA indicates more intense absorption from the photoexcited singlet states than stimulated emission. The triplet states[5,6] which are produced by spin flip are not involved in the present femtosecond experiments.

If multiple absorption/emission transitions spectrally overlap, it is not easy to determine whether ΔA stems from spectral shift (horizontal change) or population change (vertical change). As a first approximation, the zeroth moment $M_0'(t)$ which defined as the frequency average by Eq. (5) is useful to evaluate the total change of ΔA,

$$M_0'(t) = \frac{\int_{\omega_1}^{\omega_2} \Delta A(\omega,t)\mathrm{d}\omega}{\omega_2 - \omega_1}. \quad (5)$$

However, ΔA includes optical frequency dependence of the transition probability, $BI_\omega n_i$, where B is the Einstein B coefficient, I_ω is specific intensity of radiation field and n_i is the number density of molecules in quantum level i. Since I_ω depends upon the energy, integrated photon distribution over space and time of the pulse, ΔA reflects the different number of photons. It would be most fundamental to evaluate the contribution of the transition moment squared of each transition, which is proportional to B.

Therefore, we calculate the zeroth-order moment $M_0(t)$ of ΔA that is divided by the transition energy as in Eq. (6). $M_0(t)$ reflects the transition probability integrated over the photon energy range of the probe pulse. Since the spectral shape changes with time (horizontal change), it is of importance to calculate the zeroth moment to remove the 'cross talk' with intensity change (vertical change).

$$M_0(t) = \int_{\omega_1}^{\omega_2} \frac{\Delta A(\omega,t)}{\omega} \mathrm{d}\omega. \quad (6)$$

Calculated $M_0(t)$ in Fig. 2(d) displays the ultrafast decay of the total transition probability in the visible region. A sharp decrease appears in t_1 < ~100 fs and a slow increase and an even slower decrease follow in regions t_2 = 100–400 and t_3 = 400–1600 fs, respectively. There seems to be at least three decay processes. M_0 also displays vibronic fringes due to the coherent intramolecular vibrational relaxation more evidently.

Fig. 2(e) shows the FT of ΔA in the region of 0–2000 cm^{-1}. The trace at ~1030 cm^{-1} in the power spectrum is assignable to the strongest Raman-active vibration of ground-state methanol at 1035 cm^{-1} (presented in Fig. S1). However, the vibrational frequencies of 2'HC are not same as those at the ground state (Fig. S1),[55,56] since the photoexcited 2'HC molecule changes its vibrational frequencies on the way of decay processes. Detailed vibrational analyses on real-time frequency change on the excited states are discussed in Sec. 4.8.

4.2 Analyses on a sequential decay model

We can determine rate constants $k_1 - k_3$ for the three processes by fitting a decay curve at each wavelength on the 2D $\Delta A(\lambda, t_d)$ map. The decay processes are represented as A (S_3) → B → C → D (S_0*), and corresponding rate equations are given by Eqs. (7)–(10). In the present experimental time scale, component D is long lived and k_4 can be approximately regarded to be zero.

$$\frac{\mathrm{d}[A]}{\mathrm{d}t} = -k_1[\mathrm{A}], \quad (7)$$
$$\frac{\mathrm{d}[\mathrm{B}]}{\mathrm{d}t} = k_1[\mathrm{A}] - k_2[\mathrm{B}], \quad (8)$$
$$\frac{\mathrm{d}[\mathrm{C}]}{\mathrm{d}t} = k_2[\mathrm{B}] - k_3[\mathrm{C}], \quad (9)$$
$$\frac{\mathrm{d}[\mathrm{D}]}{\mathrm{d}t} = k_3[\mathrm{C}] - k_4[\mathrm{D}]. \quad (10)$$

Difference absorbance ΔA is obtained by subtracting the contribution of the ground state G from those of photoinduced species A–D as in Eq. (11),

$$\Delta A = (\varepsilon_{\mathrm{A}}[\mathrm{A}] + \varepsilon_{\mathrm{B}}[\mathrm{B}] + \varepsilon_{\mathrm{C}}[\mathrm{C}] + \varepsilon_{\mathrm{D}}[\mathrm{D}] - \varepsilon_{\mathrm{G}}[\mathrm{G}])l. \quad (11)$$

where ε_j (j = A–D and G) and l are molar absorption coefficients and the sample thickness, respectively.

The first process in the shortest delay time region is expected to be significantly fast. Thus, the apparatus function of a Gaussian function with FWHM 10 fs was convoluted with the exponential decay function. The resultant function represented with the complementary error function in Eq. (S16) was

applied for determination of τ_1 after subtracting the longer decay components. Details are given in the ESI. Since the ratio of excited 2'HC to the ground state is estimated to be 0.83 % from the laser spectrum, laser power, focused spot size, the initial concentration $[A]_0$ is set to be 8.3×10^{-4} molL^{-1}. The other initial concentrations are zero.

Fig. 3 presents determined relaxation lifetimes, rate constants, and molar absorption coefficients. The most remarkable result is the kinetic deuterium effect that appears clearly in τ_2 in Fig. 3(b) and k_2 in Fig. 3(e). Thus, proton or hydrogen atom transfer is involved in the second process. In contrast, the first and third processes display small differences between the OH and OD analogues in τ_i [i = 1 and 3, Fig. 3(a) and (c)] and k_i [Fig, 3(d) and (f)]. Since the first k_1 process is faster than the resolution of the probe pulse, a Gaussian apparatus function is convoluted with the exponential decay functions in the analyses. A special care was taken in fitting three k_i values at each wavelength by performing several types of non-linear least-squares calculations, i.e., stepwise iterative or subtraction fitting and simultaneous global fitting. The former method is found to give τ_i and k_i with smaller error. The obtained frequency-averaged lifetimes are τ_1 = 35 ± 1 fs, τ_2 = 93 ± 1 fs and τ_3 = 690 ± 9 fs for the OH analogues, and τ_1 = 38 ± 1 fs, τ_2 = 164 ± 1 fs and τ_3 = 759 ± 13 fs for the OD analogues. These ultrafast rate constants of 2'HC have been determined for the first time in this paper in a much shorter time regime than previous studies.[4-6]

The second significant point is the wavelength dependences of τ_i and k_i, which have become obtainable in the present multichannel experiments. We call them τ_i and k_i spectra, respectively. The rate constant k_1 does not depend much upon probe photon energy in the range 1.9–2.4 eV as in Fig. 3(d), whereas k_2 and k_3 show significant wavelength dependences in Fig. 3(e) and (f), respectively. The k_2 spectra in Fig. 3(e) of the OH (black) and OD (red) isotopomers show, respectively, nearly monotonic decrease and a peaked feature, whereas the k_3 spectra of both OH and OD in Fig. 3(f) display a local maximum at ~2.4 eV. The remained small isotopic differences in k_1 and k_3 may be due to numerical errors.

Fig. 3(g) shows absorption spectra of transient components A to D obtained from the $\Delta A(\lambda, t_d)$ map. Again, careful examinations were made to obtain reliable spectra by trying several fitting procedures, i.e., simultaneous global fitting and stepwise iterative fitting with respect to ε_j and k_i, and stepwise subtraction fitting for the k_1–k_3 components. The absorption spectra in the units of molar absorption coefficients ε_A to ε_D in Fig. 3(g) for the OH analogue were obtained from the stepwise independent fitting with three pre-determined rate constants k_1–k_3. The global fitting leads to essentially similar spectra. But the stepwise independent fitting with fewer fitting parameters would give more reliable ε_j spectra. Formalisms of fitting functions for obtaining the absorption coefficients are given in the ESI.

Component A involved in the k_1 process displays a broad absorption peaking at ~2.3 eV with $\varepsilon_A \approx$ 1000 – 800 mol L^{-1}cm^{-1} over the range 2.1–2.5 eV, whereas the ε_B, ε_C and ε_D spectra appear in higher

energy regions and are smaller than ε_A. The values of ε_B, ε_C, and ε_D monotonically increase with photon energy and reach 650, 500 and 100 $mol^{-1}L\ cm^{-1}$ respectively at 2.6 eV. The observed abrupt breach over the entire frequency region and subsequent high-energy shifts in Fig. 2(b) are due to ε_A and other ε_j components, respectively.

The final component D shows significantly weak absorption in this region, and there is no band in the ground state absorption of *trans*-2'HC [Fig. 1(b)] or *cis*-2'HC.[6] Therefore, component D is not due to the original ground state S_0 (component G) but thermally-populated, non-equilibrated ground state S_0*. High vibrational levels are transiently populated in the S_0 electronic state after the internal conversion, and they make the absorption red shifted from the stationary S_1-S_0 absorption in Fig. 1(b). The present multiplex experiments demonstrate the possibility of extracting such non-equilibrium dynamics of high vibrational states.

The other relaxation channel of *cis-trans* isomerization at the C1'-C9 bond could in principle take place as in Fig. 1(a). However, according to the previous experiments with a UV lamp,[4] the quantum yield to this channel is as small as 1%, compared to the main channel, and their reaction rate is only 0.1 $\%h^{-1}$ in methanol. Hence, this channel is negligible under the present experimental condition.

As discussed previously on spectral behaviour (a) and (b), time dependencies are observed differently in the regions above and below 2.25 eV in Fig. 2(c). This is due to the lack of component B in absorption below 2.25 eV as shown in Fig. 3(g). Component B increases with time constant τ_1 = 35 fs and decreases with τ_2 = 93 fs. After the process, component C contributes to the growth at 2.25 and 2.09 eV in Fig. 2(c) due to its broad band tail extending below 2.3 eV after the initial bleach.

The spectral change can be analyzed using the first moment $M_1(t)$, which is defined as the frequency-weighted average of ΔA given by Eq. (12),

$$M_1(t) = \frac{\int_{\omega_1}^{\omega_2} \omega \Delta A(\omega, t) \mathrm{d}\omega}{\int_{\omega_1}^{\omega_2} \Delta A(\omega, t) \mathrm{d}\omega}. \quad (12)$$

Fig. 2(d) presents the calculated M_1 in the region of 2.051–2.337 eV, in which the three time dependences of spectral change are involved. The change of M_1 is in parallel with that of M_0 in ranges t_1, t_2 and t_3. Namely, the initial blue shift upon excitation towards 2.25 eV in range t_1, fast red shift in range t_2 and gradual recovery in range t_3. Since τ_1 and τ_2 are determined as 35 and 93 fs, respectively, these shifts are primarily due to component B which has the absorption coefficient in higher photon energy [Fig. 3(g)]. Note that M_1 takes the mid-point value of 2.194 eV if ΔA is constant over the entire energy range.

4.3 Potential energy surfaces and decay paths

Fig. 4 presents the calculated potential energy profiles of 2'HC along the decay path after photoexcitation to $S_3(\pi_2\pi^*)$ (a) in methanol and (b) in the vacuum (isolated molecule), and also depicts the molecular orbitals of the π^*, π_1, π_2 and n types in Figs. 4(c)–4(f), respectively. The black, red, blue and green lines indicate the potential energy curves of the ground state, excited states of $\pi_1\pi^*$, $n\pi^*$ and $\pi_2\pi^*$ characters, respectively. As shown in Fig. 4(a), an ultrafast isomerization pathway in methanol is obtained as S_{3FC} (4.21 eV) → S_{3MIN} (4.03 eV) → S_3/S_2 (4.04 eV) → S_2/S_1 (3.73 eV) → $S_{1MIN\text{-}trans}$ (3.6606 eV) → $S_{1TS\text{-}taut}$ (3.6634 eV) → $S_{1MIN\text{-}taut}$ (3.16 eV) → $S_{1TS\text{-}twist}$ (3.29 eV) → S_1/S_0 (2.63 eV). The minimum of S_{3MIN} is significantly close to the intersection of S_3/S_2 in methanol in Fig. 4(a), whereas S_{3MIN} is calculated to be higher than S_3/S_2 in the vacuum in Fig. 4(b). Detailed energies of such critical points are given in Fig. S2 and S3.

After the photoexcitation at geometry S_{3FC}, 2'HC will immediately deform to S_{3MIN} because S_{3FC} and S_{3MIN} are directly connected by the meta-IRC in the S_3 state. At S_{3MIN}, following internal conversion takes place rapidly from the $S_3(\pi_2\pi^*)$ state to the $S_2(n\pi^*)$ state by passing through the S_3/S_2 region, which is geometrically and energetically close to S_{3MIN} in methanol. Then, 2'HC decays to the S_1 surface via S_2/S_1 since a meta-IRC path directly connects S_3/S_2 and S_2/S_1. Local minimum $S_{1MIN\text{-}trans}$ and transition state $S_{1TS\text{-}taut}$ are located geometrically and energetically close to S_2/S_1.

Along the reaction path $S_{1MIN\text{-}trans}$→$S_{1TS\text{-}taut}$→$S_{1MIN\text{-}taut}$, proton transfer takes place as depicted in Fig. 4, and the character of the S_1 state changes accordingly from $n\pi^*$ and $\pi_1\pi^*$ since $S_{1TS\text{-}taut}$ corresponds to an avoided crossing. Then, 2'HC overcomes the small barrier of $S_{1TS\text{-}twist}$ and finally decays to the S_0 electronic ground state surface via the S_1/S_0 region. After the proton transfer, the C1'−C9 bond twisting occurs as depicted in Fig. 4(a), and the dihedral angle C2'-C1'-C9-O10 changes from planar (17°) to perpendicular (89°). This twisting motion is likely to proceed slowly because the distance along the reaction coordinate is substantially long. Also, the motion of heavy atoms is included during the molecular geometry deformation. Based on the present calculations, three experimental decay components can be summarized as follows.

(1) The first experimental decay component A (τ_1 = 35 fs) corresponds to the process of S_{3FC}→S_{3MIN} →S_3/S_2, in which two species S_{3MIN} and S_3/S_2 are involved without clear separation. The small energy difference (0.01 eV) between S_{3MIN} and S_3/S_2 is consistent with the ultrashort lifetime τ_1.

(2) The second component B (τ_2 = 93 fs) corresponds to the proton transfer on the excited state as S_2/S_1→$S_{1MIN\text{-}trans}$→$S_{1TS\text{-}taut}$, in which again two species are involved without clear separation. The proton transfer is undoubtedly supported by the observed deuterium effect, τ_2 = 93 fs (H) → 164 fs (D). As noted above, the electronic configuration of the S_1 state changes from $n\pi^*$ to $\pi_1\pi^*$ during the proton transfer process of $S_{1MIN\text{-}trans}$→$S_{1TS\text{-}taut}$→$S_{1MIN\text{-}taut}$. This change gives rise to the spectral red shift from ε_B (>2.3 eV) dominant to ε_C dominant (with low energy tail).

(3) The decay of the third component C (τ_3 = 690 fs) is due to the C1'−C9 bond twisting on the course of $S_{1MIN\text{-}taut} \rightarrow S_{1TS\text{-}twist} \rightarrow S_0/S_1$. Conversely, the broad band tail of $\mathscr{E}_C$ leads to the ΔA increase in the energy range lower than 2.25 eV at 150–350 fs in Fig. 2(c).

4.4 Molecular polarity and solvent effects

Comparisons of calculations between in methanol and in the vacuum would present a general insight about solvent effects. The energies of the crucial points, S_2/S_1, $S_{1MIN\text{-}trans}$, $S_{1TS\text{-}taut}$, S_1/S_0, are calculated to be similar under the both conditions. The geometrical deformation in the vacuum is also similar to that in methanol along the decay path: in the process from S_{3FC} to S_3/S_2 the O11-H14 bond length increases whereas the O10-H14 distance decreases; in the process from S_3/S_2 to $S_{1MIN\text{-}trans}$ both of the O11-H14 bond and the O10-H14 distance become back to the initial values with increase of the C2'-C1'-C9-O10 dihedral angle; and in the process from $S_{1MIN\text{-}trans}$ to S_1/S_0 the twisting motion of C1'-C9 bond takes place.

The only significant difference is energy difference 0.42 eV between S_3/S_2 in methanol (4.04 eV) and S_3/S_2 in the vacuum (4.46 eV). This discrepancy can be explained by the molecular polarity. The nπ* state (blue line) has a smaller dipole moment than the ground state or the excited $\pi_1\pi^*$ and $\pi_2\pi^*$ states, and is less stabilized in the polar solvent compared to other $\pi_1\pi^*$ or $\pi_2\pi^*$ states (see Fig. S2 and S3). The calculated dipole moments in the vacuum at the S_{3FC} geometry are 6.63 Debye in $S_3(\pi_2\pi^*)$, 4.65 Debye in $S_2(\pi_1\pi^*)$, 1.69 Debye in $S_1(n\pi^*)$ and 3.99 Debye in S_0, where 1 Debye = 3.34×10^{-30} Cm. The nπ state is also less polar i.e. less stabilized along the whole decay path. As a result, the electronic configurations $S_2(n\pi^*)$ and $S_1(\pi_1\pi^*)$ in methanol are interchanged from $S_2(\pi_1\pi^*)$ and $S_1(n\pi^*)$ in the vacuum at the S_{3FC} geometry. The ground and ππ* states are more stabilized than the nπ* state during the decay, and the less stabilized nπ* state compared to the ground, $\pi_1\pi^*$ and $\pi_2\pi^*$ states in methanol gives rise to the energy difference.

4.5 Ultrafast relaxation processes

Even though the time course of the TRS is analyzed with three components A, B and C, there is no isosbestic points in the TRS [see Fig. 2(b)]. The absence of isosbestic point can be explained by the two types of contributions of spectral change (horizontal change) and intensity change (vertical change). Details are the following.

(1) The vibrational distribution in the non-equilibrated state cannot be described by the Boltzmann distribution with any temperature. The ultrafast dynamics takes place so rapidly through the reaction pathway that the spectral change cannot be described by the sum of stationary local structures. Thus, more appropriate descriptions are A ($S_{3FC} \rightarrow S_{3MIN} \rightarrow S_3/S_2$) → B ($S_2/S_1 \rightarrow S_{1MIN\text{-}trans} \rightarrow S_{1TS\text{-}taut}$) → C ($S_{1MIN\text{-}taut} \rightarrow S_{1TS\text{-}twist} \rightarrow S_1/S_0$) → D ($S_0$*), rather than A($S_{3MIN}$) → B ($S_{1MIN\text{-}$

$_{trans}$) → C ($S_{1MIN\text{-}taut}$) → D (S_0*). Here, S_0* means vibrationally non-equilibrated, electronic ground state. Sometimes it is called 'hot' ground state but we prefer non-equilibrated or equivalently non-thermal state because 'hot' should be related to some defined temperature.

(2) The spectral modulation induced by the wavepacket motion may not be decoupled because of the time-range overlap between ultrafast electronic dynamics and vibrational period. In general, real-time vibrational modulation of electronic states during the electronic relaxation is observed in femtosecond transient absorption kinetics. The present above-mentioned kinetic model involves fast sequential intermediate electronic states A–C and long-lived state D (S_0*). In such a system, a model based on the static electronic absorption spectra is valid only if the observation is made over a long enough time in which at least several vibrational periods of the coupled modes take place. Otherwise the temporal and spectral overlap of induced absorption the A–C sequential process and coexistence of induced absorption and stimulated emission would make the isosbestic points obscure.

4.6 Probe wavelength dependence

If the TR ΔA spectrum is merely a sum of population-weighted static spectra of intermediate species, the rate constants k_1, k_2 and k_3 estimated using Eqs. (7)–(10) should not depend upon the probe wavelength. In fact, k_2 and k_3 depend upon the probe wavelength as in Fig. 3(e) and (f), respectively. Here, let us postulate a model proposed in previous papers[27,57] that the decay rate constant of k_i is affected by the internal conversion through the conical intersection (CI).

$$k(E) = k_0 e^{-\left|\frac{E - E_0}{\Delta E}\right|}. \tag{13}$$

When the electronic wavepacket travels along the decay path around the CI, rate constant k takes the largest value k_0 at the center of the crossing point. Assuming the energy E_0 of absorption from the CI to the final state, the energy level E of any state can be measured with respect to the same final state. As given by Eq. (13), the decay rate constant of $k(E)$ decreases in proportional to exponential of $-|E - E_0|$ at any location above or below the CI due to the standard tunneling probability over an energy gap ΔE. Hence, when the probe wavelength matches transition energy E_0 from the conical intersection to the final excited states, the rate constant $k(E)$ becomes largest.

The local maxima in the k_2 and k_3 spectra in Fig. 3(e) and (f) respectively correspond to the maxima (fitted by blue lines) of the tunneling rate through energy barriers centered at the conical intersections S_2/S_1 and S_1/S_0 in Fig. 4(a), respectively. Table 1 presents estimated energy E_0 and width ΔE. The kinetic deuteration effect is obtained for k_2; i.e., it is 1.9 times larger in the OH analogue than in the OD analogue. In contrast, E_0 and ΔE are similar between the OH and OD analogues at both S_2/S_1 and S_1/S_0.

They essentially reflect the same electronic energy surface provided that the zero-point energy can be neglected. Transition energy E_0 from the transient state to higher electronic excited states is estimated to be ~0.1 eV larger in OD than OH at both S_2/S_1 and S_1/S_0.

The model makes it possible to discuss the location and width (or shape) of the conical intersection based on experimental evidence. The fact that tunneling width ΔE at S_2/S_1 is larger than that at S_1/S_0 indicates that the structural deformation with respect to energy change around S_2/S_1 is relatively smaller than around S_1/S_0. Furthermore, the ΔE value is slightly smaller in the OD analogue, in which the vibrational amplitude is smaller. Difference of $E_0 \approx 0.35$ eV between S_2/S_1 and S_1/S_0 correspond to the calculated energy difference 1.10 eV between 3.73 and 2.63 eV in Fig. 4(a). A possible reason for this discrepancy is difference in the final states of probing transitions S_m-S_2 and S_n-S_1, where S_m and S_n being higher excited states.

4.7 Equal-pulse-type DUV pump - probe experiments

Fig. 5(a) and (b) present a 2D display of $\Delta A(\omega, t_d)$ and slices of frequency spectra for the equal-pulse-type experiments[58] using DUV pump and DUV probe in the region of 4.43–4.88 eV. Stimulated emission gives negative ΔA below 4.6 eV in Fig. 5(b) since the DUV probe pulse overlaps the $S_3 \leftarrow S_0$ absorption below ~4.6 eV as shown in Fig. 1(b). The negative ΔA also means a smaller cross-section of absorption from the photoinduced excited states than that of the stimulated emission to the ground state. On the other hand absorption of transient species are observed as positive ΔA in the region above 4.6 eV, where the ground state absorption is almost absent in Fig. 1(b) and the transient absorption exceeds the stimulated emission. The shapes of the spectra at various probe delay times in Fig. 5(b) are similar to each other.

Fig. 5(c) shows the time dependences of $\Delta A(\omega, t_d)$ at probe energy $\hbar\omega$ = 4.76, 4.70, 4.64 and 4.59 eV, respectively. The fast k_1 and k_2 processes cannot be observed due to disturbance by coherent spikes in the region 0–150 fs. Therefore, it is difficult to extract the ultrafast spectral dynamics in this delay time region. In the remaining delay time range $t_d \geq$ 150 fs, all of the ΔA traces display similar monotonic increases. Fitting with two exponential functions plus a constant was found to give either similar relaxation times or significantly unbalanced relaxation times. Therefore, a single exponential function plus a constant in Eq. (14) is employed and the relaxation time τ_1' = 647 fs was obtained as the photon energy average of Fig. 5(d). This value is fairly close to estimated τ_3 of the C=C rotation in Sec. 4.3, i.e., this time dependence corresponds to the formation of the twisted structure after the proton transfer process of $S_{1MIN\text{-}taut} \rightarrow S_{1TS\text{-}twist} \rightarrow S_1/S_0$ in Fig. 4(a).

$$\Delta A = \Delta A_1 e^{-\frac{t}{\tau_1'}} + \Delta A_\infty \quad (14)$$

Fig. 6(a) presents transient absorption spectra obtained as ΔA_1 and ΔA_∞ from the 2D ΔA map of Fig. 5(a) assuming $\tau_1' = 647$ fs in Eq. (14). In particular, ΔA_1 component shows the effect of negative absorption. This bleaching is partly due to population loss of the ground state and to the stimulated emission. The former is estimated to be 4.3 % based on the laser spectrum, laser power, focused spot size and sample concentration. Fig. 6(b) displays the final reconstructed spectra, in which the effects from the population loss, stimulated emission and the ultrafast population decay (vertical change) of the $S_3 \rightarrow S_0$ are excluded.

The contribution from the ultrafast population decay is explained as follows. 2'HC decays nonradiatively to the S_2 state within 35 fs after the photoexcitation to S_3. The S_1-S_0 transition is off-resonant with the probe photon energy. Hence, the rapid decay from the S_3 state to S_2/S_1 results in the effective cancellation of the $S_3 \rightarrow S_0$ stimulated emission contribution to the signals. Both of ΔA_1 and ΔA_∞ display strong absorption at the low energy side in Fig.6(b). This spectral shape corresponds to component D (S_0*).

4.8 Coherent dynamics of molecular vibrations

The real-time vibronic modulation can be studied using the spectrogram analysis.[11,59] Fig. 7(a) shows a spectrogram $S(\nu, t_d)$ in the region of 200–1000 fs, which is obtained from FT of a time trace of ΔA in a sliding-time window of the Blackman function with the FWHM of 400 fs. The shape and width of the gate function is determined with special care of avoiding interference with neighbouring modes.[10,11,60] The black line in $S(\nu, t_d)$ represents the peak of spectrogram amplitude at each gate delay time, and corresponds to an *instantaneous* vibrational frequency of the dephasing molecules. This type of modulation can be observed in various molecular systems.[12,61]

In Fig. 7(b), similar analyses are applied to a low frequency region, and a frequency peak of 87 cm^{-1} is clearly obtained along with a peak of 225 cm^{-1} with a small FT power. Fig. 7(b) corresponds to the Fourier power spectrum of the instantaneous frequency distribution as in Fig. 7(a). The obtained peaks in Fig. 7(a) and (b) are the frequencies of vibrational modes which are vibronically excited by molecular geometry deformation during the decay process after the S_3 excitation. In Fig. 7(a), the instantaneous frequency changes in a range 1550–1600 cm^{-1}. The frequency peak firstly decreases from 1650 cm^{-1} at 200 fs to 1530 cm^{-1} at 450 fs, and increases again to 1620 cm^{-1} at 650 fs. It should be reminded that the time scale of the spectrogram in Fig. 7(a) is restricted by the averaging time window of 400 fs in this analysis. These modes are coupled to the molecular deformations and impulsively excited along the decay path.

The fact that the lifetime of the vibrational modulation is less than 800 fs in Fig. 7(a) is consistent with those in the transient absorption spectra, $\tau_1 = 35$ fs, $\tau_2 = 93$ fs and $\tau_3 = 690$ fs. The vibrational

modulation is understood based on the molecular geometry deformations in the process from S_{3FC} to $S_{1MIN\text{-}taut}$ shown in Fig. 4(a).

The normal modes that are relevant to the decay path can be determined by comparing them with the molecular geometry deformations along S_{3FC}, S_{3MIN}, S_3/S_2, S_2/S_1, $S_{1MIN\text{-}trans}$, $S_{1TS\text{-}taut}$ and $S_{1MIN\text{-}taut}$. As shown in Fig. 4(a), the molecular geometry significantly changes in the C7-C8 bond length (1.344 Å–1.383 Å) and the dihedral angle of C2'-C1'-C9-O10 (0°–40°). It follows that the C7-C8 bond stretching motion and the C1'-C9 bond twisting motion are enhanced during the decay path from S_{3FC} to $S_{1MIN\text{-}taut}$.

The distance of O11-H14 and O10-H14 also change significantly in connection with the proton transfer. However, the vibrational frequency of OH stretch ~3000 cm^{-1} is out of the spectrogram, and we do not discuss here. The reason for the missing of the frequency range higher than 2000 cm^{-1} is insensitivity of if any frequency modulation due to their short vibrational periods (<15 fs) which are close to the experimental time resolution of 12 fs.

4.9 Normal mode analyses

Normal mode analyses are carried out on the three minima, S_{3MIN}, $S_{1MIN\text{-}trans}$ and $S_{1MIN\text{-}taut}$, at the TDDFT level of theory with CPCM (methanol). There are several normal modes in the range from 1500 cm^{-1} to 1700 cm^{-1} at S_{3MIN}, $S_{1MIN\text{-}trans}$ and $S_{1MIN\text{-}taut}$. The most relevant normal modes which have the largest contribution to the C7-C8 bond stretching motion are chosen by a normal-mode displacement analysis. They possess vibrational frequencies of 1647 cm^{-1} (S_{3MIN}, τ_1 = 35 fs), 1591 cm^{-1} ($S_{1MIN\text{-}trans}$, τ_2 = 93 fs) and 1623 cm^{-1} ($S_{1MIN\text{-}tau}$, τ_3 = 690 fs). The normal mode displacements are depicted in Fig. S4(a), (b) and (c), respectively. In the previous paper, the vibrational frequency of C7-C8 stretch has been calculated around 1550 cm^{-1} and 1600 cm^{-1},[55,56] which is consistent with the present results.

Although the calculated vibrational frequencies are slightly higher than observation due to the lack of anharmonic effect in the calculations, the trend of the vibrational modulation is successfully reproduced; e.g., the peak frequency decreases first and increases again. Also, the time dependence of the vibrational modulation in Fig.7 (a) is consistent with the determined lifetimes $\tau_1-\tau_3$. Therefore, it is concluded that the observed spectrogram peak modulation in Fig. 7(a) corresponds to the vibrational modulation of C7-C8 stretch, which is enhanced during the decay process.

In a low-frequency range 70–150 cm^{-1}, only two normal modes are obtained on S_{3MIN}, $S_{1MIN\text{-}trans}$ and $S_{1MIN\text{-}taut}$. Their vibrational frequencies are 89 and 122 cm^{-1} at S_{3MIN}, 93 and 107 cm^{-1} at $S_{1MIN\text{-}trans}$ and 84 and 110 cm^{-1} at $S_{1MIN\text{-}taut}$. Their normal-mode displacements include the twisting motion of the C1'-C9 bond, as depicted in Fig. S4(d), (e) and (f), respectively. These results explain satisfactorily the observed spectrogram peak of 87 cm^{-1} shown in Fig. 7(b).

In a range 220–290 cm^{-1}, two normal modes are also obtained on S_{3MIN}, $S_{1MIN\text{-}trans}$ and $S_{1MIN\text{-}taut}$. These normal modes involve bending motion of the molecular plane, as depicted in Fig. S4(g), (h) and (i),

respectively. Therefore, the spectrogram peak at 225 cm^{-1} with a small FT power corresponds to the bending modes which are weakly enhanced by the twisting motion along the decay path.

5. Conclusions

The ultrafast dynamics of DUV photoexcited 2'HC has been determined for the first time. The ultrafast processes are summarized as follows. The first spectral changes take place due to the internal conversion through conical interactions S_3/S_2 and S_2/S_1, and explained by lifetime τ_1 = 35 fs. The proton transfer occurs subsequently, as confirmed by the experimental evidence of kinetic deuteration effects on the dynamics. The internal conversion S_3/S_2 and S_2/S_1 are strongly expected from the DFT calculations in Fig. 4. Otherwise the S_1 state cannot undergo the proton transfer that takes place only on the S_1 state. 2'HC undergoes the proton transfer before C1'-C9 rotation with time constant τ_2 = 93 fs before *cis-trans* isomerization at the ring. The last process is the C=C twist with τ_3 = 690 fs. Even after the relaxation to the ground electronic state, isomerization towards flavanone in the time range longer than 1.6 ps has not been observed in the present experimental time scale. The real-time vibronic motion has been observed as the spectrogram. The observed instantaneous frequency modulation has been successfully reproduced by normal-mode analyses along the decay path.

Conflicts of interest

There are no conflicts to declare.

Acknowledgements

The authors thank Masaya Suzuki, Taichi Tanaka and Arkadiusz Jarota for their help during experiment. TK was supported by JST, ICORP 'Ultrashort Pulse Laser Project' and by JST, CREST 'Fusion of High Performance Optical Science and Technology, Photo Imaging with High Performance Lasers', 2014–2018. YH was supported by JST, PRESTO with Grant Number JPMJPR16N8. SM was supported by JST, CREST with Grant Number JPMJCR14L5. A part of the results was computed at the computer center of Kyoto University. YY was supported by JSPS through Kakenhi Grant Number JP16K05645.

References

1 R. Prasath, P. Bhavana, S. Sarveswari, S. W. Ng and E. R. T. Tiekink, *J. Mol. Struct.*, 2015, **1081**, 201–210.

2 K. Zenger, S. Dutta, H. Wolff, M. G. Genton and B. Kraus, *Toxicology*, 2015, **336**, 26–33.

3 N. A. Shakil, M. K. Singh, M. Sathiyendiran, J. Kumar and J. C. Padaria, *Eur. J. Med. Chem.*, 2013, **59**, 120–131.

4 R. Matsushima and H. Kageyama, *J. Chem. Soc., Perkin Trans.*, 1985, **2**, 743–748.

5 P. T. Chou, M. L. Martinez and W. C. Cooper, *J. Am. Chem. Soc.*, 1992, **114**, 4943–4944.

6 Y. Norikane, H. Itoh and T. Arai, *J. Phys. Chem. A*, 2002, **106**, 2766–2776.

7 Ø. M. Andersen and K. R. Markham, *Flavonoids: Chemistry, Biochemistry and Applications*, CRC Press, 2005.

8 K. Yoshida, M. Mori and T. Kondo, *Nat. Prod. Rep.*, 2009, **26**, 884–915.

9 T. Kobayashi, T. Saito and H. Ohtani, *Nature*, 2001, **414**, 531–534.

10 I. Iwakura A. Yabushita, J. Liu, K. Okamura, S. Kezuka and T. Kobayashi, *Pure Appl. Chem.*, 2013, **85**, 1991–2004.

11 J. Du and T. Kobayashi, *Chem. Phys. Lett.*, 2009, **481**, 204–208.

12 Z. Wang, T. Otsubo and T. Kobayashi, *Chem. Phys. Lett.*, 2006, **430**, 45–50.

13 T. Fuji, T. Saito and T. Kobayashi, *Chem. Phys. Lett.*, 2000, **332**, 324–330.

14 H. Kano, T. Saito and T. Kobayashi, *J. Phys. Chem. A*, 2002, **106**, 3445–3453.

15 T. Kobayashi and H. Kano, *Nonlinear Opt. Quant. Opt.* 2004, **31**, 115.

16 R. Matsushima, H. Mizuno and H. Itoh, *J. Photochem. Photobio. A*, 1995, **89**, 251–256.

17 Y. Leydet, P. Batat, G. Jonusauskas, S. Denisov, J. C. Lima, A. J. Parola, N. D. McClenaghan and F. Pina, *J. Phys. Chem. A*, 2013, **117**, 4167–4173.

18 F. Pina, M. J. Melo, M. Maestri, R. Ballardini and V. Balzani, *J. Am. Chem. Soc.*, 1997, **119**, 5556–5561.

19 Y.-B. Jiang, X.-J. Wang and L. Lin, *J. Phys. Chem.*, 1994, **98**, 12367–12372.

20 K. Rurack, M. L. Dekhtyar, J. L. Bricks, U. Resch-Genger and W. Rettig, *J. Phys. Chem. A*, 1999, **103**, 9626–9635.

21 K. Rurack, J. L. Bricks, G. Reck, R. Radeglia and U. Resch-Genger, *J. Phys. Chem. A*, 2000, **104**, 3087–3109.

22 W. Rettig, W. Majenz, R. Herter, J.-F. Letárd and R. Lapouyade, *Pure Appl. Chem.*, 1993, **65**, 1699–1704.

23 R. J. DeVoe, M. R. V. Sahyun and E. Schmidt, *Can. J. Chem.*, 1989, **67**, 1565–1575.

24 Y. Wang, *J. Phys. Chem.*, 1985, **89**, 3799–3805.

25 P.Wang and S. Wu, *J. Photochem. Photobio. A*, 1995, **86**, 109–113.

26 T. Kobayashi and Y. Kida, *Phys. Chem. Chem. Phys.*, 2012, **14**, 6200–6210.

27 B. Xue, A. Yabushita and T. Kobayashi, *Phys. Chem. Chem. Phys.*, 2016, **18,** 17044–17053.

28 Y. Kida, K. Okamura, J. Liu and T. Kobayashi, *Appl. Opt.*, 2012, **51**, 6403–6410.

29 Y. Kida, J. Liu and T. Kobayashi, *Appl. Phys. B*, 2011, **105**, 675–679.

30 R. R. Alfano, *The Supercontinuum Laser Source*, Springer, Berlin, 1989.

31 N. Ishii, E. Tokunaga, S. Adachi, T. Kimura, H. Matsuda and T. Kobayashi, *Phys. Rev. A*, 2004, **70**, 023811.

32 E. Runge and E. K. U. Gross, *Phys. Rev. Lett.*, 1984, **52**, 997–1000.

33 M. E. Casida, in *World Scientific: Singapore*, ed. by D. P. Chong, World Scientific, Singapore, 1995, pp. 155–192.

34 S. Maeda, Y. Harabuchi, Y. Ono, T. Taketsugu and K. Morokuma, *Int. J. Quantum Chem.*, 2015, **115**, 258–269.

35 J. D. Chai and M. Head-Gordon, *J. Chem. Phys.*, 2008, **128**, 084106.

36 A. D. Laurent and D. Jacquemin, *Int. J. Quantum Chem.*, 2013, **113**, 2019–2039.

37 Y. H. Shao, M. Head-Gordon and A. I. Krylov, *J. Chem. Phys.*, 2003, **118**, 4807–4818.

38 F. Wang and T. Ziegler, *J. Chem. Phys.*, 2004, **121**, 12191–12196.

39 N. Minezawa and M. S. Gordon, *J. Phys. Chem. A*, 2009, **113**, 12749–12753.

40 S. Maeda, Y. Harabuchi, T. Taketsugu and K. Morokuma, *J. Phys. Chem. A*, 2014, **118**, 12050–12058.

41 S. Maeda, Y. Harabuchi, M. Takagi, T. Taketsugu and K. Morokuma, *Chem. Rec.*, 2016, **16**, 2232–2248.

42 S. Maeda, T. Taketsugu and K. Morokuma, *J. Comput. Chem.*, 2014, **35**, 166–173.

43 A. D. Becke, *Phys. Rev. A*, 1988, **38**, 3098–3100.

44 C. T. Lee, W. T. Yang R. G. Parr, *Phys. Rev. B*, 1988, **37**, 785–789.

45 A. Klamt and G. Schuurmann, *J. Chem. Soc., Perkin Trans.*, 1993, **2**, 799–805.

46 J. Andzelm, C. Kolmel and A. Klamt, *J. Chem. Phys*., 1995, **103**, 9312–9320.

47 V. Barone and M. Cossi, *J. Phys. Chem. A*, 1998, **102**, 1995–2001.

48 M. Cossi, N. Rega, G. Scalmani and V. Barone, *J. Comput. Chem.*, 2003, **24**, 669–681.

49 M. J.Frisch, G. W. Trucks, H. B. Schlegel, G. E. Scuseria, M. A. Robb, J. R. Cheeseman, G. Scalmani, V. Barone, B. Mennucci, G. A. Petersson, H. Nakatsuji, M. Caricato, X. Li, H. P. Hratchian, A. F. Izmaylov, J. Bloino, G. Zheng, J. L. Sonnenberg, M. Hada, M. Ehara, K. Toyota, R. Fukuda, J. Hasegawa, M. Ishida, T. Nakajima, Y. Honda, O. Kitao, H. Nakai, T. Vreven, J. A. Montgomery, Jr., J. E.Peralta, F. Ogliaro, M. Bearpark, J. J. Heyd, E. Brothers, K. N. Kudin, V. N. Staroverov, R. Kobayashi, J. Normand, K. Raghavachari, A. Rendell, J. C. Burant, S. S. Iyengar, J. Tomasi, M. Cossi, N. Rega, J. M. Millam, M. Klene, J. E. Knox, J. B. Cross, V. Bakken, C. Adamo, J. Jaramillo,

R. Gomperts, R. E. Stratmann, O. Yazyev, A. J. Austin, R. Cammi, C. Pomelli, J. W. Ochterski, R. L. Martin, K. Morokuma, V. G. Zakrzewski, G. A. Voth, P. Salvador, J. J. Dannenberg, S. Dapprich, A. D. Daniels, O. Farkas, J. B. Foresman, J. V. Ortiz, J. Cioslowski and D. J. Fox, Gaussian 09, revision A.1, Gaussian, Inc., Wallingford CT, 2016.

50 M. S. Gordon and M. W. Schmidt, In *Theory and Applications of Computational Chemistry: The First Forty Years*, Ed. by C. Dykstra, G. Frenking, K. Kim and G. Scuseria, Elsevier, Amsterdam, The Netherlands, 2005.

51 M. W. Schmidt, K. K. Baldridge, J. A. Boatz, S. T. Elbert, M. S. Gordon, J. H. Jensen, S. Koseki, N. Matsunaga, K. A. Nguyen, S. J. Su, T. L. Windus, M. Dupuis and J. A. Montgomery, *J. Comput. Chem.*, 1993, **14**, 1347–1363.

52 S. Maeda; Y. Harabuchi; Y. Sumiya; M. Takagi; M. Hatanaka; Y. Osada; T. Taketsugu; K. Morokuma; Ohno, K., GRRM (a developmental version), Hokkaido University, 2017. (see http://grrm.chem.tohoku.ac.jp/GRRM/index_e.html [accessed on March 3, 2016], GRRM14)

53 R. Matsushima and I. Hirao, *Bull Chem. Soc. Jpn.*, 1980, **53**, 518–522.

54 *Handbook of HeI Photoelectron Spectra of Fundamental Organic Molecules*, K. Kimura, S. Katsumata, Y. Achiba, T. Yamazaki and S. Iwata, Japan Scientific Societies Press, 1981.

55 S. Prabu, R. Nagalakshmi, J. Balaji and P. Srinivasan, *Spectrochimica Acta A*, 2014, **129**, 114–120.

56 M. Jagadeesh, M. Lavanya, B. H. Babu, K. Hong, R. Ma, J. Kim and T. K. Kim, *Spectrochimica Acta A*, 2015, **150**, 557–564.

57 T. Kobayashi, M. Yasuda, S. Okada, H. Matsuda and H. Nakanishi, *Chem. Phys. Lett.* 1997, **267**, 472–480.

58 A. J. Taylor, D. J. Erskine and C. L. Tang, *Appl. Phys. Lett.* 1983, **43**, 989–991.

59 T. Kobayashi, *Bull. Chem. Soc. Jpn.*, 2013, **86**, 167–182.

60 A. Yabushita, C.-H. Kao, Y.-H. Lee and T. Kobayashi, *Chem. Lett.*, 2010, **39**, 1283–1284.

61 A. Colonna, A. Yabushita, I. Iwakura and T. Kobayashi, *Chem. Phys.*, 2007, **341**, 336–343.

Table 1. Experimentally-determined rate constant k_i and energy width ΔE at conical intersections S_2/S_1 and S_1/S_0, respectively.

	S_2/S_1		S_1/S_0	
	OH	OD	OH	OD
Rate constant k_i / ps^{-1}	13.1	6.89	1.79	1.53
E_0 / eV	1.98	2.10	2.40	2.42
ΔE / eV	0.83	0.65	0.52	0.43

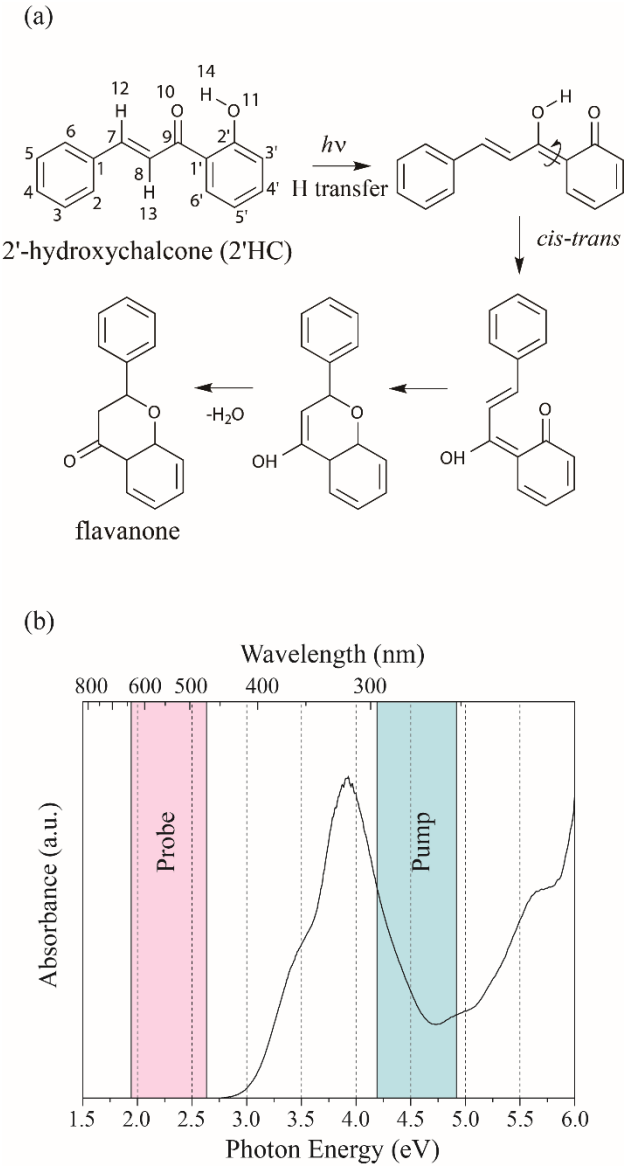

Fig. 1 (a) Photochemistry of *trans*-2'-hydroxychalcone (2'HC). (b) Electronic absorption spectra of *trans*-2'HC in methanol.

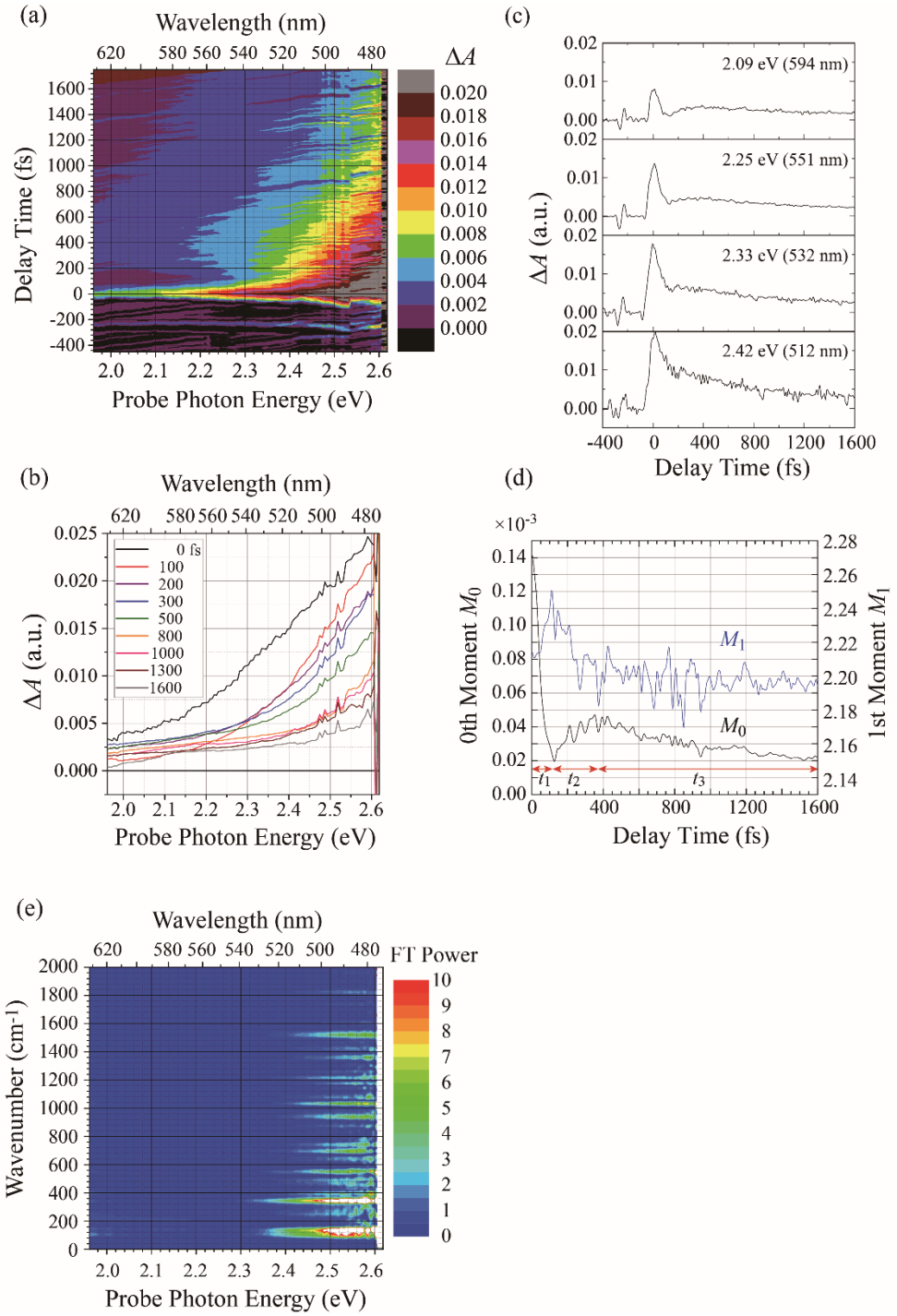

Fig. 2 (a) Two-dimensional difference absorption spectrum $\Delta A(\omega, t_d)$ with pump on and off for *trans*-2'-hydroxychalcone (2'HC) in methanol. (b) Spectral change of ΔA at nine delay times. (c) Time dependence of ΔA. (d) Temporal change of 0th and 1st order moment M_0 and M_1 in the region of 2.051−2.337eV. (e) Spectrogram $S(\nu, t)$ in a sliding-time window of 400 fs.

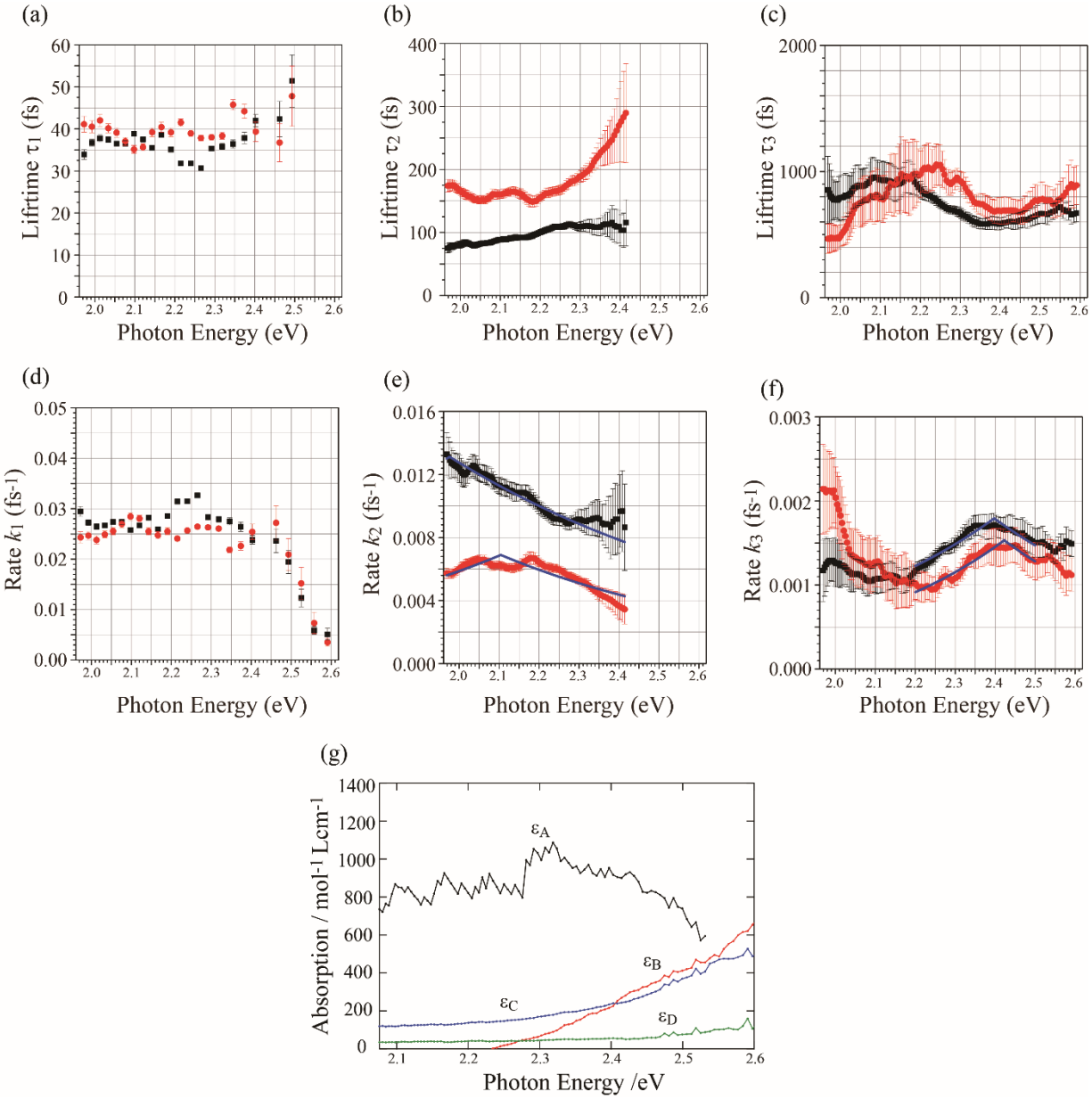

Fig. 3 (a)–(f) Experimentally determined lifetimes τ_1–τ_3 and rate constants k_1–k_3 assuming sequential processes for $\Delta A(\omega, t_d)$. Black and red symbols correspond to OH and OD analogues, respectively. (g) Determined molar absorption coefficients ε_A–ε_D (see text for A–D) .

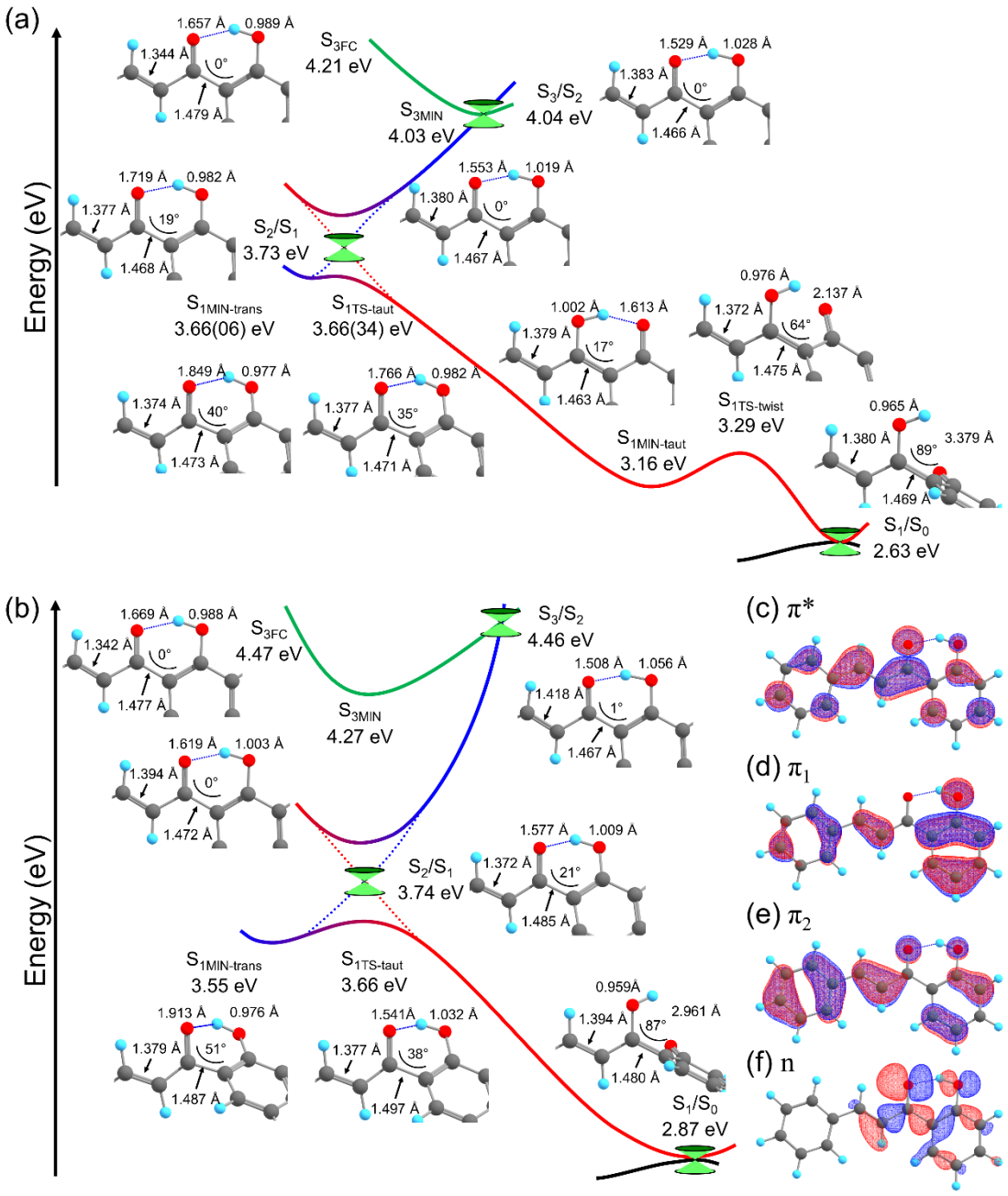

Fig. 4 Schematic potential energy profile of the decay path after photoexcitation to S_3 state for 2'-hydroxychalcone (2'HC) (a) in methanol and (b) in the vacuum. Red, blue and green lines correspond to the electronic configurations of $\pi_1\pi^*$, $n\pi^*$ and $\pi_2\pi^*$, respectively. The potential energy curves around S_2/S_1 and $S_{1TS\text{-}taut}$ are avoided crossing, and depicted by blue and red mixed lines. S_1/S_0 were computed at the SF-TDDFT/BHHLYP/6-31G(d) level, whereas the other geometries were at the ωB97XD/6-31G(d) level. The key geometrical parameters are indicated. Optimized geometries and variation of energies at the crusial points in methanol and in the vacuum are given in Table S1, S2 and Fig. S2, S3, respectively. (c)−(f) Molecular orbitals of π^*, π_1, π_2 and n at the S_{0MIN} geometry, respectively.

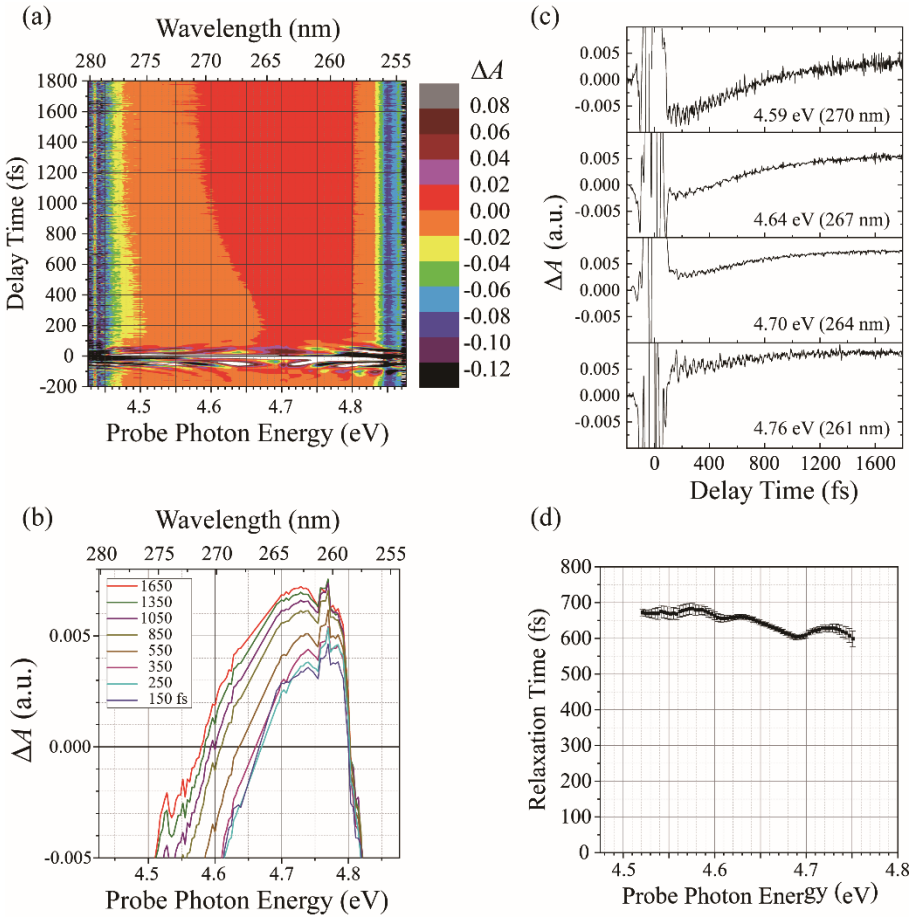

Fig. 5 (a) Two-dimensional difference absorption spectrum $\Delta A(\omega, t_d)$ with pump on and minus off for *trans*-2'-hydroxychalcone (2'HC) in methanol. (b) Spectral change of ΔA at eight delay times. (c) Delay time dependence of ΔA. (d) Experimentally determined lifetimes t_1'.

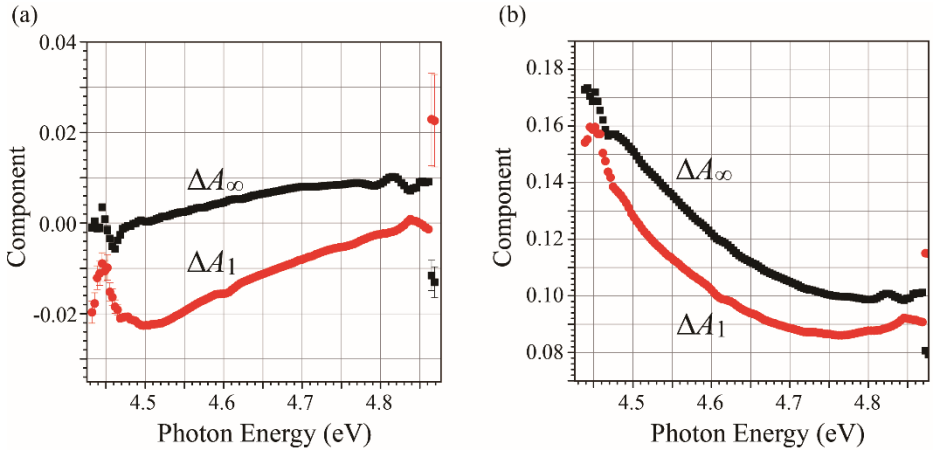

Fig. 6 Absorption components ΔA_1 and ΔA_∞ estimated using Eq. (14). The effects from population loss, stimulated emission and ultrafast population decay are excluded from (a) and resultant spectra is (b).

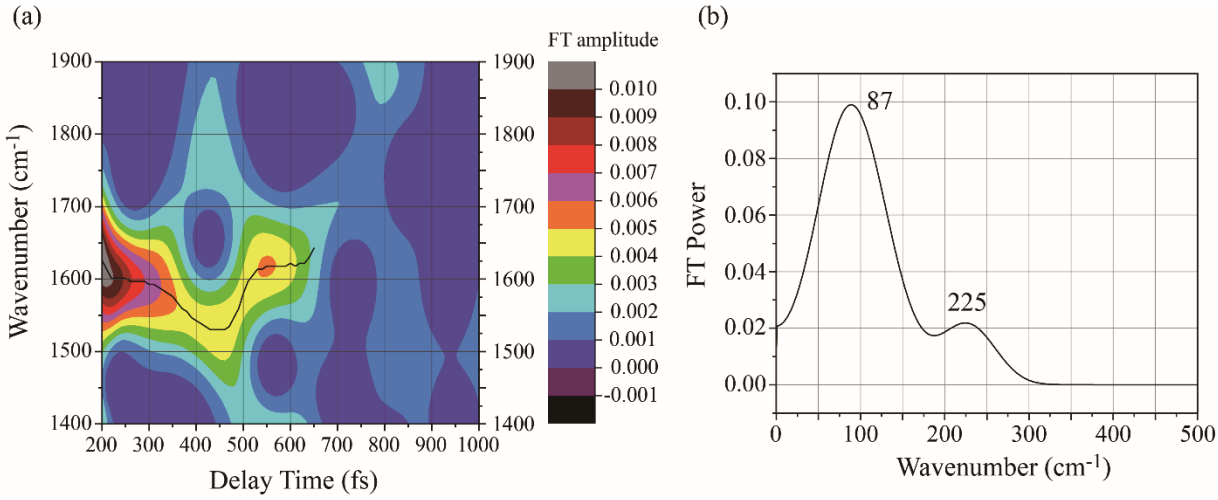

Fig. 7 Spectrogram $S(\nu, t)$ showing real-time vibrational frequency dynamics in *trans*-2'-hydroxychalcone (2'HC).